

Supplementary Information

MOF-Derived Nickel Cobaltite: A Pathway to Enhanced Supercapacitor Performance

Periyasamy Sivakumar¹, Jayaraman Balamurugan², C. Justin Raj³, Palaniappan Subramanian⁴,
Antony Dennyson Savariraj¹, Ramu Manikandan⁵, Hyun Jung^{1,*}

¹*Advanced Functional Nanohybrid Material Laboratory, Department of Chemistry, Dongguk University Seoul-Campus, Jung-gu, Seoul, 04620, Republic of Korea.*

²*National Creative Research Initiative Center for Multi-Dimensional Directed Nanoscale Assembly, Department of Material Science and Engineering, Korea Advanced Institute of Science and Technology (KAIST), Daejeon, 34141 Republic of Korea.*

³*Department of Physics, School of Advanced Sciences, Vellore Institute of Technology (VIT), Chennai Campus, Chennai - 600 127, Tamilnadu, India.*

⁴*New Technologies - Research Center, University of West Bohemia, Plzeň 30100, Czech Republic*

⁵*Department of Energy and Materials Engineering, Dongguk University Seoul-Campus, Jung-gu, Seoul, 04620, Republic of Korea.*

*Corresponding Author: chemphile@dongguk.edu (Hyun Jung)

Material characterizations

The surface morphology of the prepared electrodes was investigated using field emission scanning electron microscopy (SEM; JEOL JSM-6700F Field Emission). The transmission electron microscope (TEM) and high-resolution TEM (HRTEM; JEOL JEM-F200) equipped with a selected area diffraction pattern (SAED) were used to inspect the intrinsic morphology and structure characteristics of the obtained electrode materials. The information on the elemental distribution of the synthesized materials was examined by STEM-energy dispersive X-ray spectroscopy (EDS) mapping. The crystalline phase of the obtained products was studied using an X-ray diffraction (XRD) pattern (Ultima IV, Rigaku X-ray diffractometer). The nitrogen (N₂) adsorption/desorption isotherms (Belsorp mini II system at 77 K) were investigated to determine the BET surface area and information about the pore size distribution of the prepared materials. The chemical compositions and valence states of the synthesized materials were inspected by X-ray photoelectron spectroscopy (XPS; NOVA, Axis Technology).

2.2 Electrochemical measurements

The electrochemical characteristics of the prepared individual electrodes were analyzed using a three-electrode setup with an electrochemical workstation (BioLogic SP-150e, France). The NCO electrodes were employed as the working electrode for analyzing the electrochemical performance. Meanwhile, the Hg/HgO and Pt coil were the reference and auxiliary electrodes, respectively. The electrochemical tests for all three electrodes were conducted in an aqueous electrolyte of 6M KOH at room temperature. The working electrode was fabricated as follows: the active material, carbon black, and poly(vinylidene fluoride) (PVDF) were mixed with a mass ratio of 7:2:1 and dispersed in N-methyl-2-pyrrolidinone, respectively. The acquired slurry was applied onto a precleaned 1 cm × 1 cm area of Ni foam. The coated foam was dried at 80 °C overnight in

an electric oven. The mass of active material loaded onto the foam was estimated to be ~2 mg. The electrochemical properties of the material were analyzed using various techniques, including cyclic voltammetry (CV), galvanostatic charge-discharge (GCD), and electrochemical impedance spectroscopy (EIS). The EIS was conducted using an open-circuit potential in the frequency range between 100 kHz and 0.01 Hz.

The equation used for calculating the specific capacity C_s (mAh g⁻¹) of the NCOs synthesized in the three-electrode system can be expressed as follows:¹⁻³

$$C_s = \frac{2}{mV} \int iV(t)dt \quad (1)$$

where i stands for the constant galvanostatic discharge current, t represents the discharging time for a full discharge, m signifies the active material's mass, and region of the galvanostatic discharge plateau is indicated by $\int V(t)dt$.

2.3 Fabrication of HSC system

The HSC was assembled utilizing the hierarchical sheet-like NCO-A nanostructure as the positive electrode material, while the negative electrode material was made of commercial AC (MSP20). To maximize the electrochemical performance of HSCs, we optimized the voltage window and mass ratio of NCO-A nanostructure to AC. The optimal values were found to be 1.5 V and ~0.81, respectively. By maintaining this mass ratio, the HSC was configured with a total active mass of ~3 mg. The mass of the NCO-A nanostructure that was integrated with the AC electrodes underwent alteration, which can be expressed through the given equation:

$$\frac{m_+}{m_-} = \frac{C_- \times V_-}{C_+ \times V_+}$$

(2)

where m represents mass, C indicates specific capacitance, and V denotes the voltage range for positive (+) and negative (-) electrodes.

To verify the HSC (NCO-A//AC) in energy storage for practical applications, specific capacitance, the energy and power densities of the device were calculated using equations (3), (4), and (5) ^{1,3}.

$$C_{sp} = \frac{2}{mV^2} \int iV(t)dt \quad (3)$$

$$ED = \frac{1}{M} \int iV(t)dt \quad (4)$$

$$PD = \frac{ED}{\Delta t} \quad (5)$$

where ED (Wh kg^{-1}) represents the energy density, PD (W kg^{-1}) denotes the power density of the HSC, $\int V(t)dt$ signifies the region under the galvanostatic discharge plateau, M signifies the active material's mass, and Δt (s) indicates the discharge time.

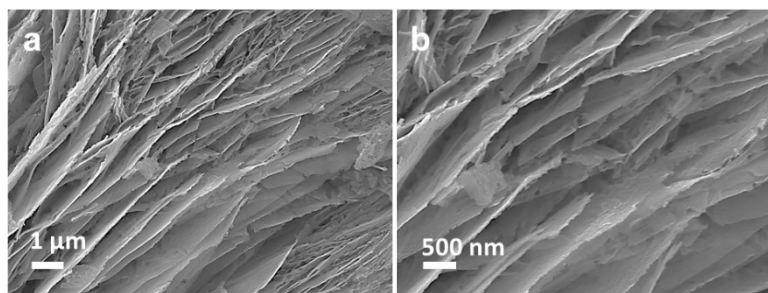


Figure S1. SEM images of hierarchical sheet-like NCO-A nanoarchitecture.

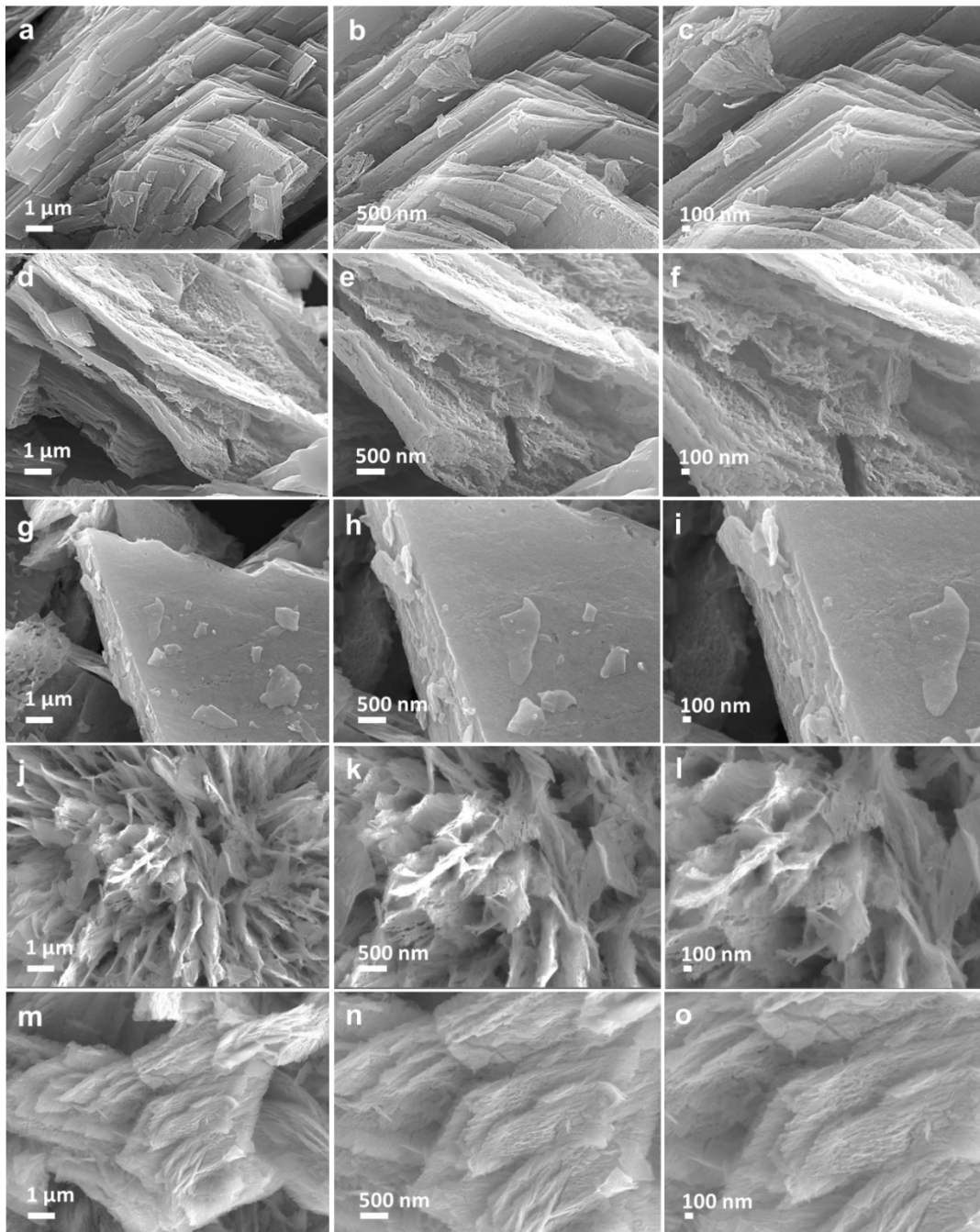


Figure S2. SEM images of (a-c) NCO-B, (d-f) NCO-C, (g-i) NCO-D, (j-l) NCO-E, and (m-o) NCO-F nanomaterials.

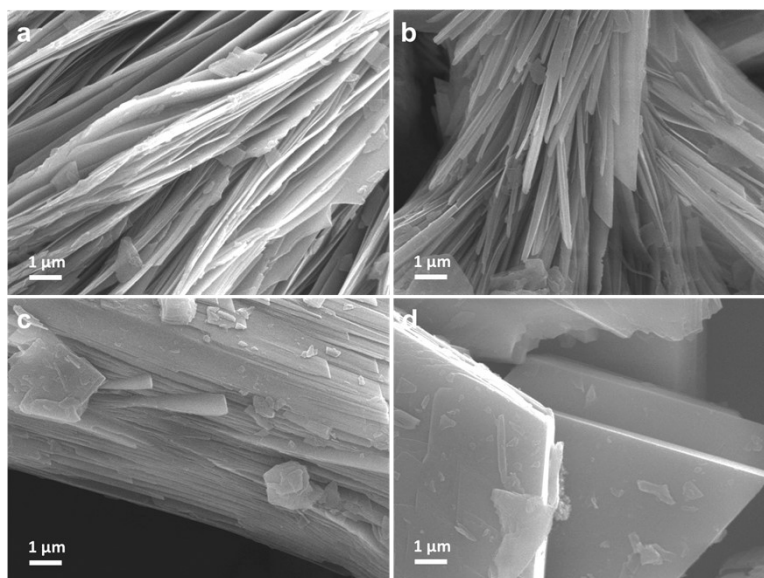


Figure S3. SEM images of (a) NiCoMOF-A, (b) NiCoMOF-B, (c) NiCoMOF-C, and (d) NiCoMOF-D nanomaterials.

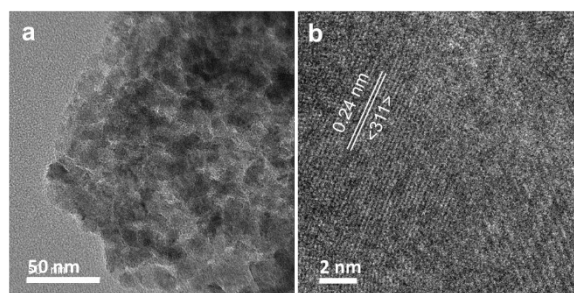


Figure S4. (a) TEM image and (b) HRTEM image of hierarchical sheet-like NCO-A nanoarchitecture.

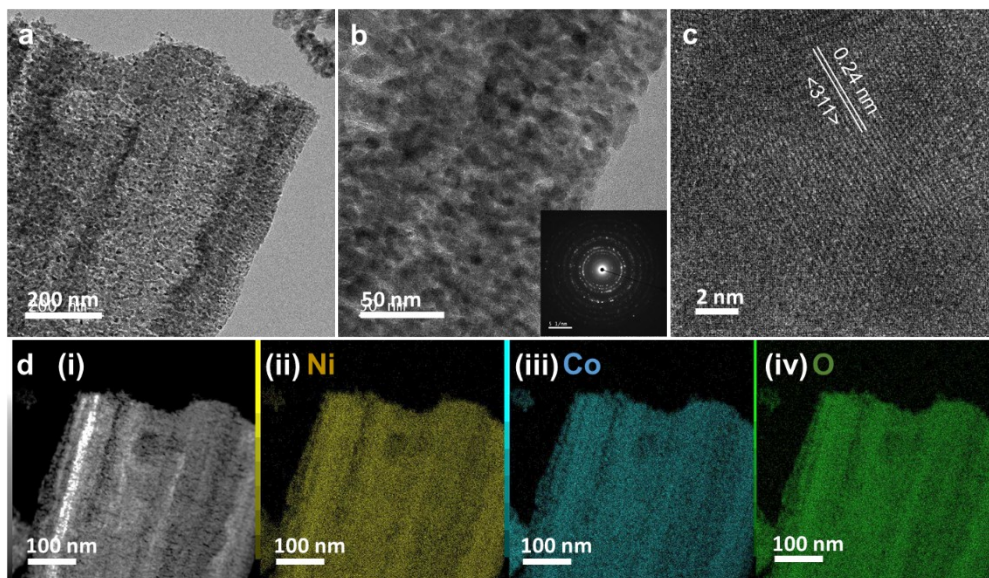


Figure S5. (a and b) TEM images (inset shows SAED pattern), (c) HRTEM image, and (e) STEM with the corresponding EDS mapping of Ni, Co, and O of stacked sheet-like NCO-B nanostructure.

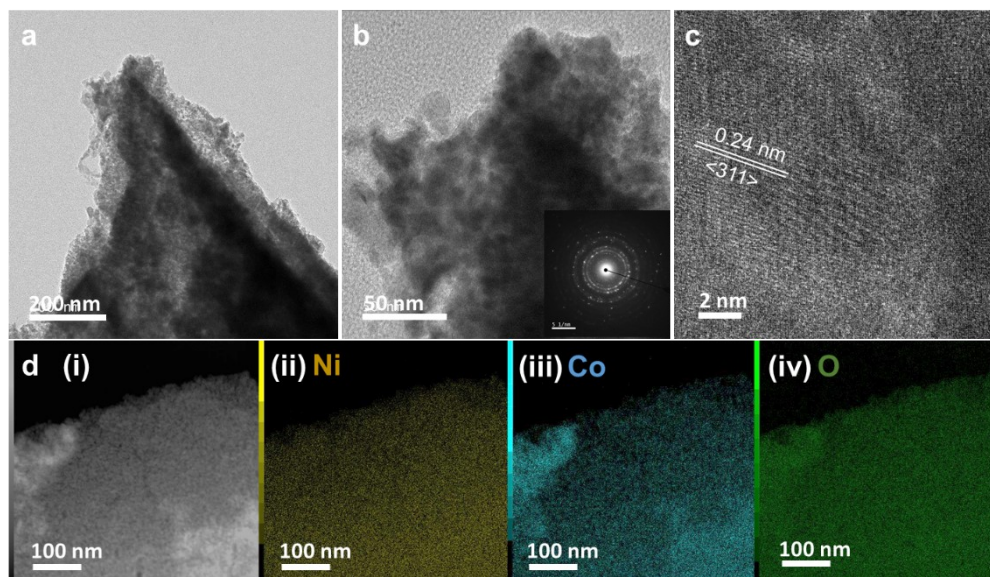


Figure S6. (a and b) TEM images (inset shows SAED pattern), (c) HRTEM image, and (e) STEM with the corresponding EDS mapping of Ni, Co, and O of NCO-C nanostructure.

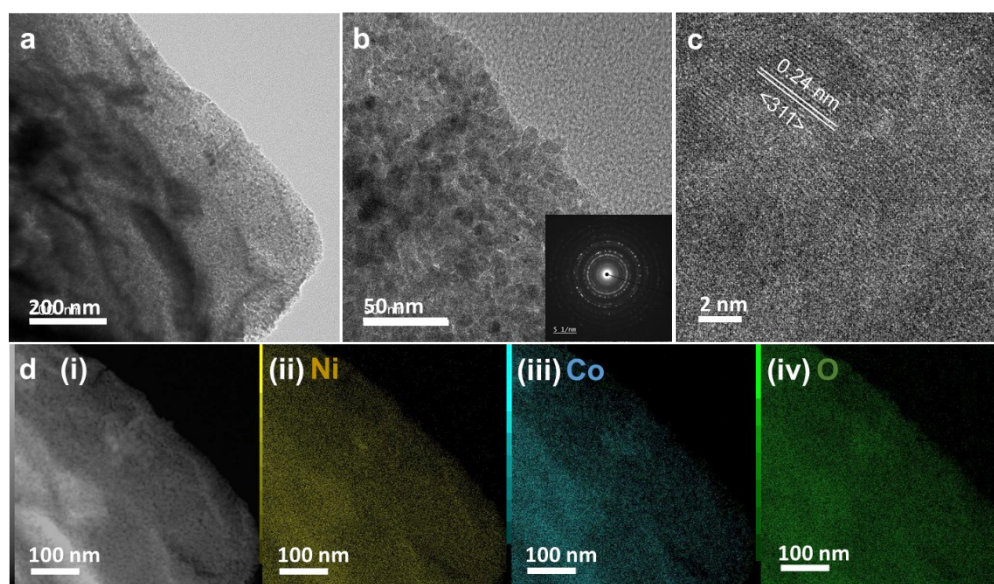


Figure S7. (a and b) TEM images (inset shows SAED pattern), (c) HRTEM image, and (e) STEM with the corresponding EDS mapping of Ni, Co, and O of NCO-D nanostructure.

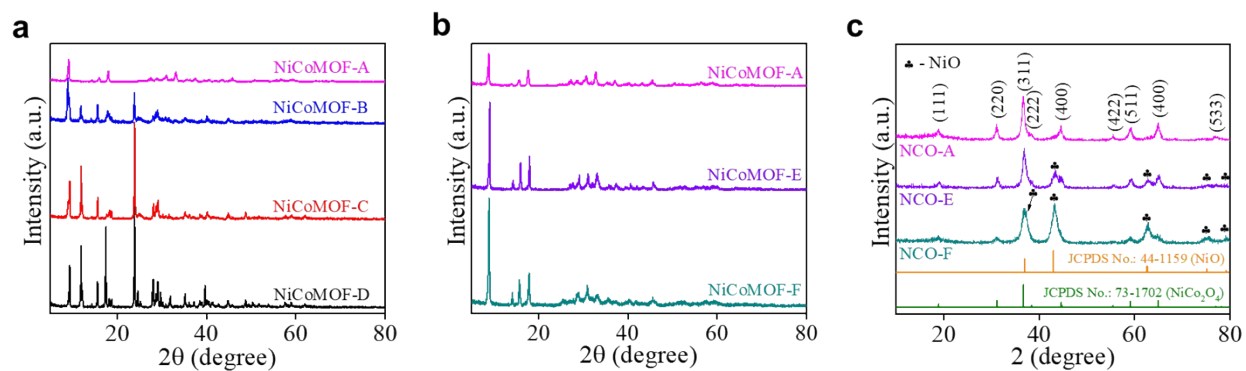


Figure S8. XRD patterns: (a) NiCoMOF-A, NiCoMOF-B, NiCoMOF-C, and NiCoMOF-D nanomaterials, (b) NiCoMOF-A, NiCoMOF-E, and NiCoMOF-F nanomaterials, and (c) NCO-A, NCO-E, and NCO-F nanomaterials.

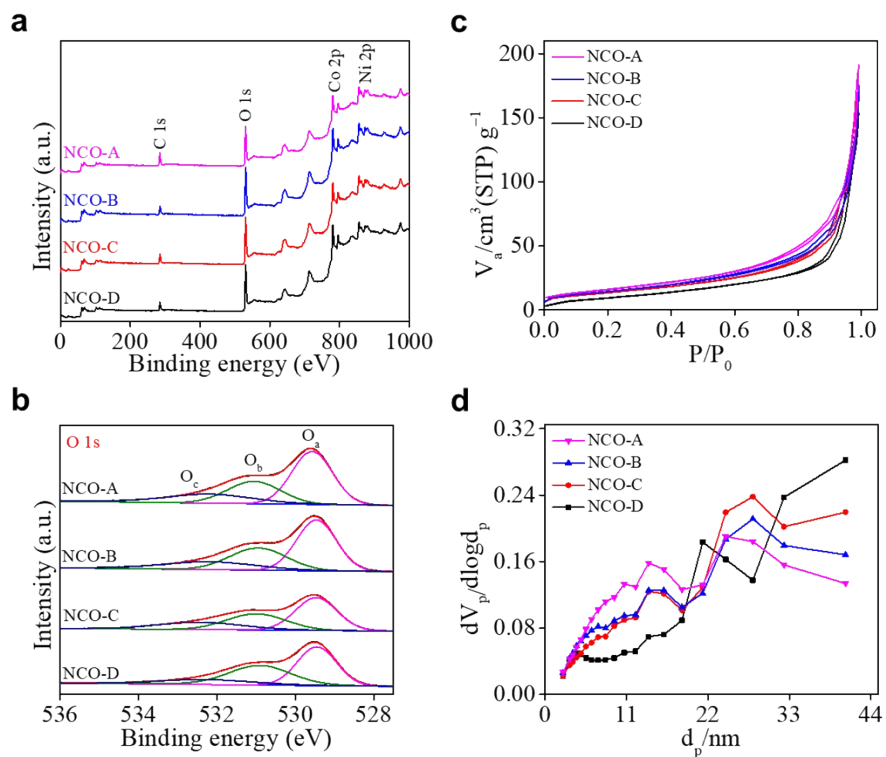


Figure S9. (a) XPS survey spectra, (b) O 1s XPS, (c) BET, and (d) pore size distribution plots NCO-A, NCO-B, NCO-C, and NCO-D nanomaterials.

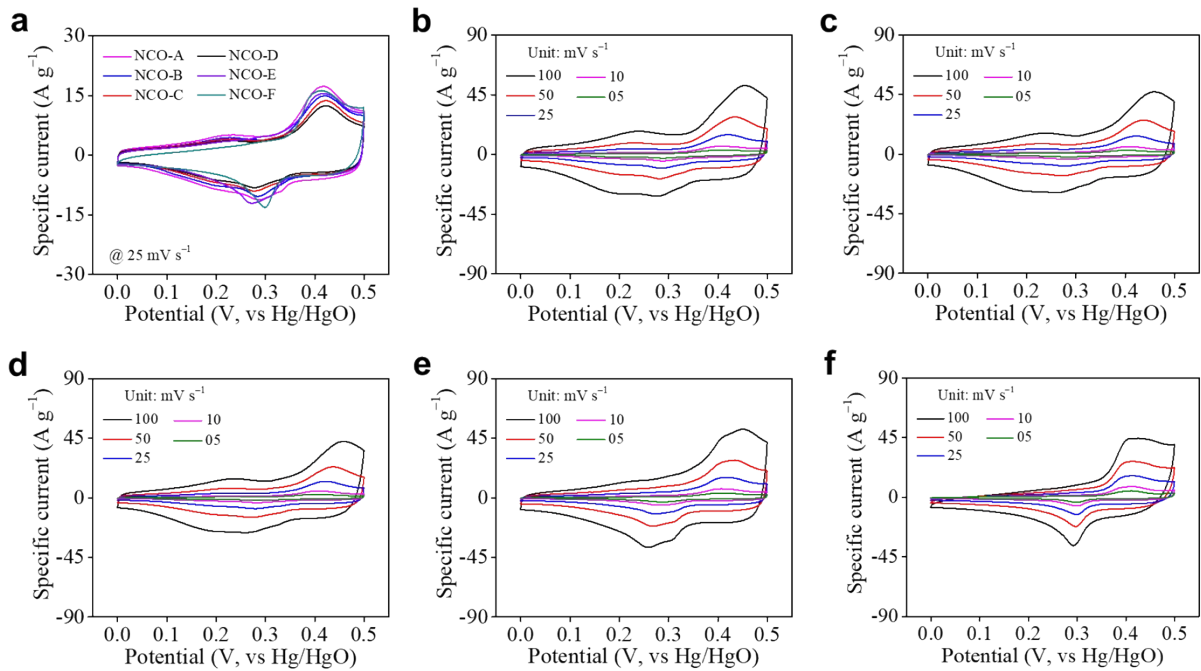


Figure S10. (a) Comparative CVs of NCO-A, NCO-B, NCO-C, NCO-D, NCO-E, and NCO-F electrodes, CVs at various sweep rates of (b) NCO-B, (c) NCO-C, (d) NCO-D, NCO-E, and NCO-F electrodes.

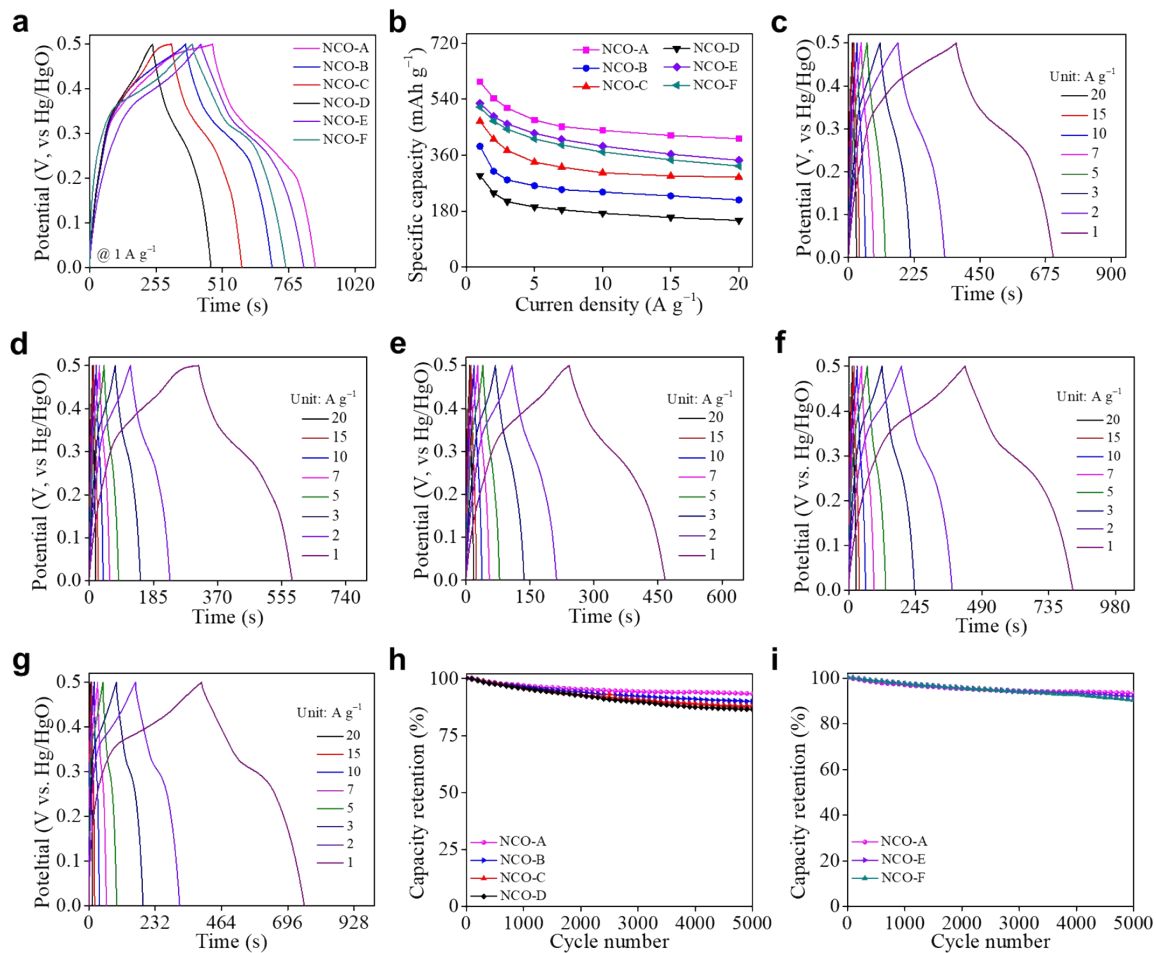


Figure S11. (a) Comparative CVs of NCO-A, NCO-B, NCO-C, NCO-D, NCO-E, and NCO-F electrodes, (b) resultant capacity as a function of the different current density of NCO-A, NCO-B, NCO-C, NCO-D, NCO-E, and NCO-F electrodes, GCD profiles at different current densities of (c) NCO-B, (d) NCO-C, (e) NCO-D, (f) NCO-E, and (g) NCO-F electrodes, and (h and i) cyclic stability of performance of NCO-A, NCO-B, NCO-C, NCO-D, NCO-E, and NCO-F electrodes.

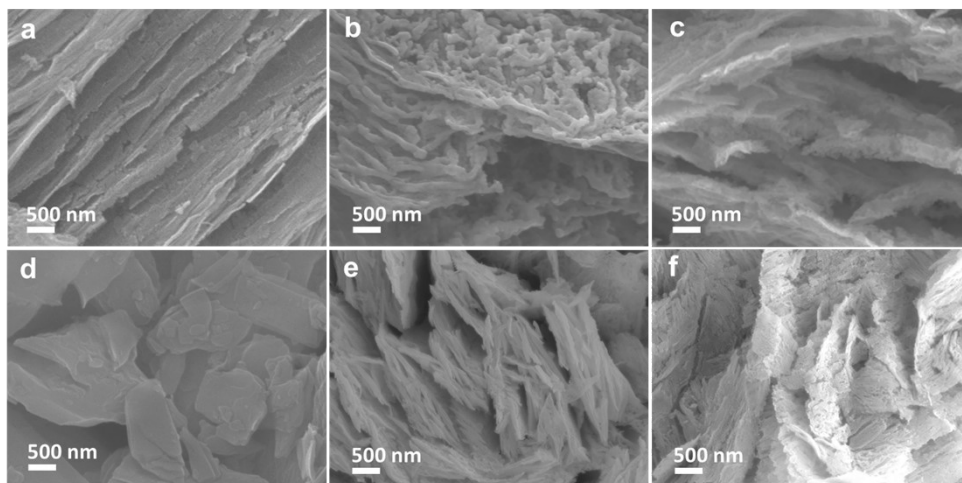


Figure S12. SEM images of the (a) NCO-A, (b) NCO-B, (c) NCO-C, (d) NCO-D, (e) NCO-E, and (f) NCO-F electrodes at different magnifications after 10000 GCD cycles.

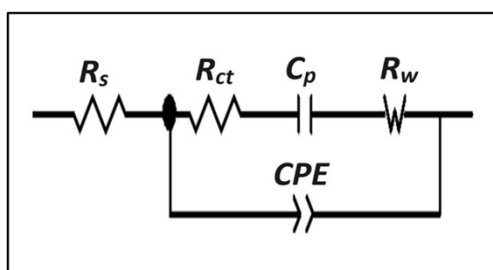


Figure S13. Equivalent circuit of fit.

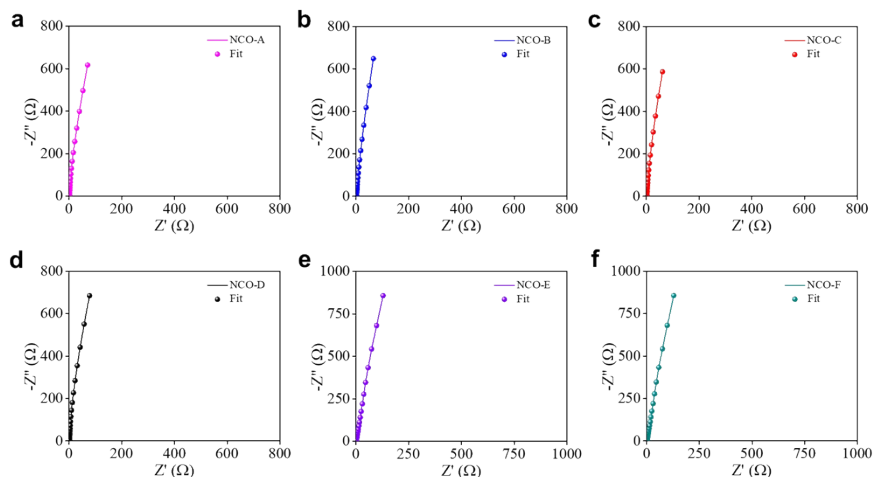


Figure S14. Nyquist plots with fitted data of (a) NCO-A, (b) NCO-B, (c) NCO-C, (d) NCO-D, (e) NCO-E, and (f) NCO-F electrodes.

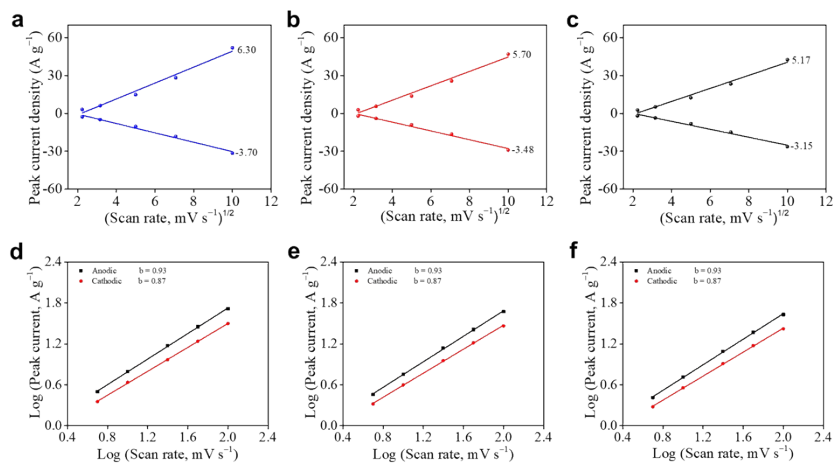


Figure 15. Peak current as a square root of scan rates: (a) NCO-B, (b) NCO-C, and (c) NCO-D nanomaterial electrodes, and Power law profile ($\log(I)$ vs. $\log(v)$) at various sweep rates: (d) NCO-B, (e) NCO-C, and (f) NCO-D electrodes.

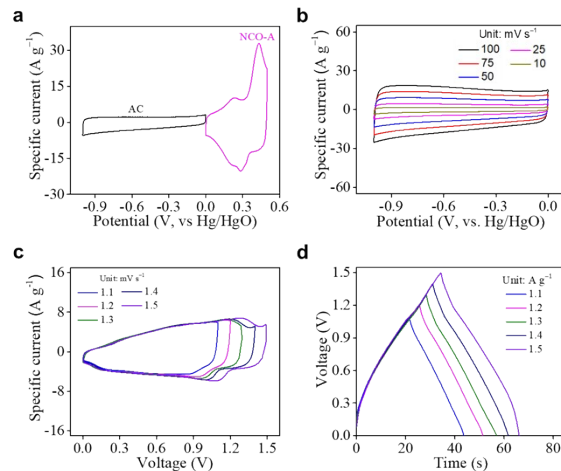


Figure S16. (a) CVs of the activated carbon (AC; MSP20) and hierarchical NCO-A electrodes at a scan rate of 50 mV s⁻¹, (b) CVs of AC at different scan rates, (c) CVs at diverse voltage windows ranging from 1.1 V to 1.5 V of HSC, and (d) GCD profiles at different voltage windows ranging from 1.1 V to 1.5 V of HSC.

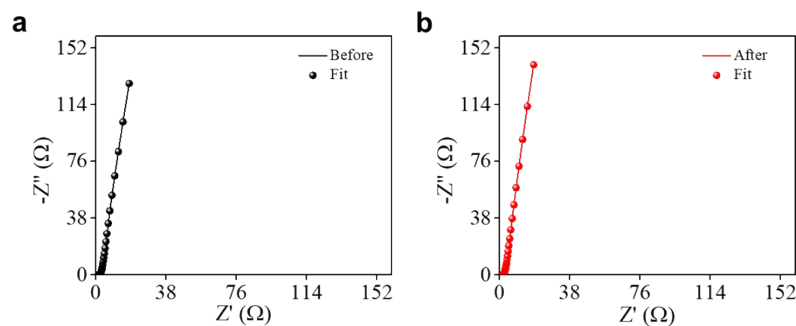


Figure S17. Nyquist plots of NCO-A//AC HSC with fitted data for (a) before and (b) after the stability test.

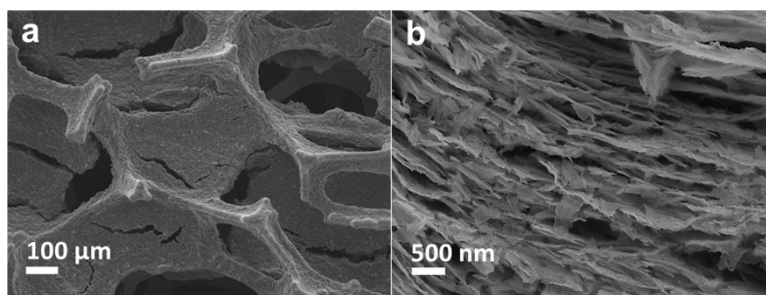


Figure S18. Different magnification SEM images of the NCO-A electrode after 10000 cycles.

Table ST1 EIS Fitted parameters of three-electrode systems.

Materials	R_s (Ω)	R_{ct} (Ω)	C_{dl} (F cm⁻²)	C_p (F cm⁻²)	R_w (Ω m)
NCO-A	0.7087	0.5267	0.00157	0.02161	1.477
NCO-B	0.7643	0.8083	0.00151	0.02053	4.286
NCO-C	0.8435	0.8377	0.00207	0.02236	2.329
NCO-D	0.8873	0.8789	0.00168	0.01949	2.223
NCO-E	0.7268	0.6136	0.00161	0.02187	1.836
NCO-F	0.7394	0.7275	0.00164	0.02237	1.961

Table ST2 EIS Fitted parameters of NCO-A//AC HSC before and after cyclic stability test.

HSC	R_s (Ω)	R_{ct} (Ω)	C_{dl} (F cm⁻²)	C_p (F cm⁻²)	R_w (Ω m)
Before stability	1.199	0.4575	0.00216	0.01012	6.114
After stability	1.189	0.4610	0.00192	0.00928	8.068

Table ST3. The performance of HSCs with various binary metal oxides reported previously is compared.

Sl. No.	Materials	Energy density (Wh kg⁻¹)	Power density (W kg⁻¹)	References
1	P-NiCo ₂ O ₄ //AC	40.0	750.0	4
2	Ni-Mn@C//3D rGO	24.1	88.8	5
3	NiCo ₂ O ₄ @Nb ₂ CT _x //AC	45.4	163.0	6
4	CoMn ₂ O ₄ NCP//AC	38.5	408.0	7
4	A-CoWO ₄ //AC	27.5	1031.4	8
5	LSMFO55//rGO	38.0	800.0	9
6	MVO-HMWCNTs//AC	26.6	385.6	10
7	NCO-A//AC	47.3	908.2	This work

References

- 1 P. Sivakumar, M. Jana, M. G. Jung, A. Gedanken and H. S. Park, *J. Mater. Chem. A*, 2019, **7**, 11362–11369.
- 2 Y. A. Dakka, J. Balamurugan, R. Balaji, N. H. Kim and J. H. Lee, *Chemical Engineering Journal*, 2020, **385**, 123455.
- 3 P. Sivakumar, C. J. Raj, H. Jung and H. S. Park, *Journal of Energy Storage*, 2023, **69**, 107946.
- 4 B. Yin, L. Hao, T. Wei, C. Wang, B. Zhu, X. Li and Q. Yang, *Journal of Power Sources*, 2022, **533**, 231409.
- 5 W. Li, W. Zhang, S. Hao and H. Wu, *Langmuir*, 2023, **39**, 12510–12519.
- 6 B. Shen, X. Liao, X. Hu, H.-T. Ren, J.-H. Lin, C.-W. Lou and T.-T. Li, *J. Mater. Chem. A*, 2023, **11**, 16823–16837.
- 7 R. Abazari, S. Sanati, A. Morsali and D. P. Dubal, *J. Mater. Chem. A*, 2021, **9**, 11001–11012.
- 8 Y. Sun, S. Liu, N. Huang, X. Wang, J. Liu, J. Bi, J. Zhang, L. Guo and X. Sun, *Journal of Power Sources*, 2022, **545**, 231911.
- 9 P. M. Shafi, D. Mohapatra, V. P. Reddy, G. Dhakal, D. R. Kumar, D. Tuma, T. Brousse and J.-J. Shim, *Energy Storage Materials*, 2022, **45**, 119–129.
- 10 B. N. V. Krishna, S. K. Hussain and J. S. Yu, *Journal of Power Sources*, 2021, **506**, 230193.